Mining, Metallurgy & Exploration (2020) 37:153–165
https://doi.org/10.1007/s42461-019-00144-1

Ground-Penetrating Radar for Karst Detection in Underground Stone Mines

Jonathan Baggett[1] · Amin Abbasi[1] · Juan Monsalve[1] · Richard Bishop[1] · Nino Ripepi[1] · John Hole[1]

Received: 1 March 2019 / Accepted: 8 October 2019 / Published online: 1 December 2019

Abstract
This work focuses on the operational and safety issues associated with karst voids in large opening underground mines. Issues include water inrush, structural instability, and engineering uncertainty in these environments. Coupled with the fracturing prevalent in folded sedimentary rocks, karst voids are complex and challenging ground-control risks. Traditional methods of predicting karst void locations, such as probe drilling, are impeded by the inconsistent spatial distribution and variable sizes of the features as reported by Li et al. (J Rock Mechan Geotech Eng:232–242, 2010) and Hassan et al. (Procedia Chem 19:737–742, 2016). Ground-penetrating radar (GPR) is a geophysical technique that transmits radio waves into a medium and subsequently detects reflected waves via a receiver. The travel time and energy of received signals are then processed and interpreted. The difference in conductivity and dielectric permittivity between limestone and open karst cavities causes strong reflections. GPR is frequently used as a geophysical surveying technique in several industries; however, there is a lack of published research on underground mining GPR applications as reported by Zhao et al. (2015a; Geophys J Int:62–71, 2015b) and Eskelinen and Pellinen (Constr Build Mater:888–898, 2018). The purpose of this work is to demonstrate the use of GPR in an underground stone mine and to discuss the importance of karst void detection ahead of mining.

Keywords Ground Penetrating Radar · Underground Mining · Karst · GPR · LiDAR

1 Introduction

The Mine Safety and Health Administration (MSHA) currently lists 116 active underground stone mines in the USA, and the vast majority of which extract limestone for crushed stone products. These limestone mines have the potential to encounter karst voids at some point in their operation, as most karstic regions of the USA develop in limestone rock masses [11]. Karsts voids, the cavities formed by the dissolution of carbonate rock, have long plagued the mining and tunneling industries, as well as been a hindrance on the Earth's surface, producing sinkholes and ruining otherwise valuable land for construction and public use. The impact of karstification on the Gavarres tunnel in Spain is well documented by Alija et al. [1]; constant instability conditions, material spills into the tunnel, and unexpected cavities seriously delayed the project deadlines and "were not foreseen in the design" [1]. At the water supply project in Sohngua River, China, Bin et al. detail the presence of both water and sediment filled karst cavities which are sources of disastrous conditions at this tunnel [4]. A hydrological tunnel in Lebanon encountered numerous massive karst voids in the tunneling path which required remediation via friction anchors, rockbolts, welded wire fabric, channel steel arch segments, invert steel beams, and shotcrete [12]. From a design standpoint, rock mass classification schemes, such as the RMR from Bieniawski and the Q-system from Barton, are not able to represent the true nature of a karstified carbonate rock mass, and therefore, complex case-by-case analyses of underground conditions are necessary [2].

Ground-penetrating radar (GPR) has been well understood and frequently employed in geophysical research studies since its first uses in glacier studies of Stern in 1930 [18]. With applications ranging from rebar detection in concrete structures to buried grave identification in historical cemeteries, GPR's unique advantages have been widely identified and utilized [18]. The first sophisticated GPR system was constructed by Geophysical Survey Systems, Inc. and its benefit was demonstrated by surveying ice-cored hills in Tuktoyaktuk, Canada [3]. Today in 2018, a wealth of knowledge in the form of textbooks, scholarly articles, and case

✉ Jonathan Baggett
jonb4@vt.edu

[1] Virginia Tech, Blacksburg, VA, USA

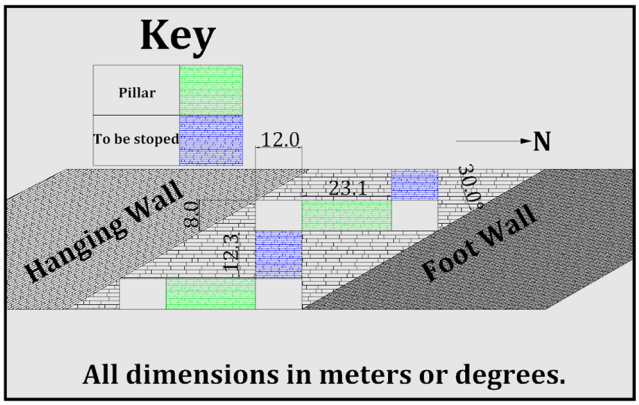

Fig. 1 Mine model

Fig. 3 Hanging-wall side of triangular pillar

studies exists that has evolved the straightforward radar technology into a well-respected 3D imaging tool and quantitative estimator of medium properties [18].

Through electromagnetic wave propagation, GPR systems are capable of accomplishing the detection of dielectric boundaries within a solid medium, such as a rock mass or concrete structure. Conductive mediums highly attenuate the GPR wave energy, such as wet clays and soils, while dry, homogenous, resistive mediums are ideal for strong transmitted and received signals [3]. Working in both ideal and problematic mediums, GPR has been demonstrated to map fractures in ornamental gneiss [7], map soil stratigraphy, and bedrock depth [5], and even to determine surface electrical properties on Mars and the Moon [17]. The most common modern use of GPR is in concrete and asphalt imaging for construction and civil engineering uses, detecting the locations of rebar and metal structures as well as paving thickness and discontinuities [8].

There are many successful examples of GPR being used in tunnels to predict conditions ahead of the working face and tunnel boring machine. Weidong et al. [20] demonstrate with a 100-MHz system the detection of loose rock due to blasting, broken up rock 18 m behind the working face, and fissure water [20]. Wang et al. [19] conducted a GPR survey on the walls of a tunnel to detect vertical shafts successfully [19]. NIOSH has conducted research demonstrating GPR's capability to detect the extent of the spread of grout pumped into a tunnel roof, a common ground-control technique and hazard remediation practice in tunneling and mining [14]. In his extensive doctoral dissertation, Kovin [10] details his uses of GPR in potash mines to map stratigraphy, estimate the thickness of the overlying water-protective beds, characterize fractures, detect unstable roof rock, and evaluate the integrity of supporting pillars in the potash rock. These studies assert the viability of GPR as a monitoring and investigative tool in underground excavations.

At this case study mine, management personnel indicated that it would be advantageous for their operation if they could use GPR at an active face for geologic forecast. Their blasting design would benefit if voids could be detected roughly 5–10 m beyond the face.

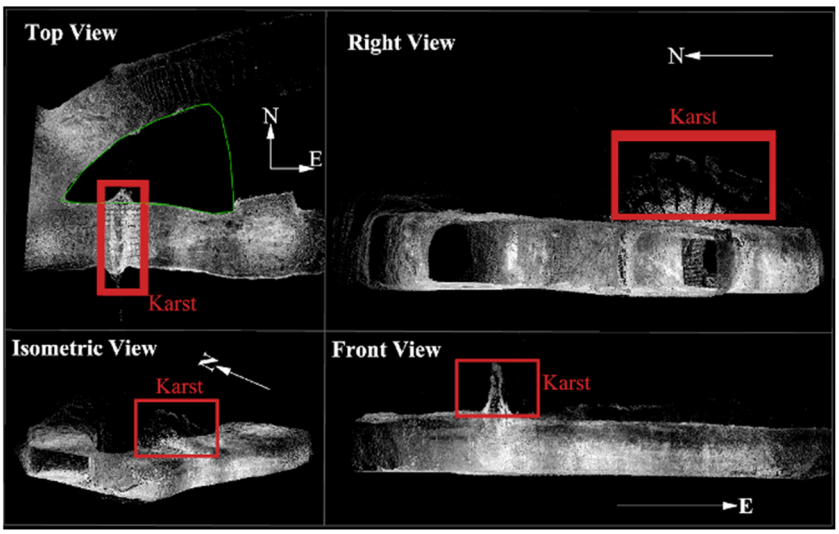

Fig. 2 Views of case-study pillar and karst void

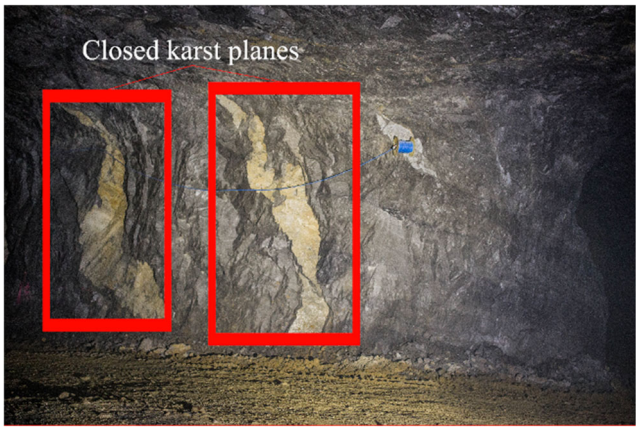

Fig. 4 Foot-wall side of triangular pillar

Fig. 6 Low-frequency survey setup

2 Methodology

2.1 Case Study Mine

The case-study mine for GPR surveying is an underground multi-level room and pillar limestone mine. The ore body is synclinal, dipping at 30°; at present, and the deepest level of the mine is approximately at the bottom of the syncline. The limestone orebody is roughly 30 m thick. The current tunneling design allows for two 12-m-wide, 8-m-tall tunnels separated by 24-m-wide square pillars to safely extract as much of the seam as possible. As shown in Fig. 1, the rock between the hanging-wall tunnel of an upper level and the foot-wall tunnel of the level below is eventually completely stopped. This mining method is appropriate for most of the upper levels of the mine; however, adjustments to the number of tunnels and necessary pillar orientations are obvious in the lower levels where the dip of the orebody flattens and the syncline bottoms out.

Karst voids are found throughout the rock mass with spatial frequency that varies from level to level. These voids range in size from centimeter-scale width to several hundred cubic meter volumes. They are typically planar and perpendicular to the mine tunneling direction; debris, consisting of residual clay and rock blocks, caves into the mining tunnel when production blasts breach the void. Figure 2 shows a laser scan taken within a mine tunnel around a pillar and directly underneath of a protected void opening in the tunnel roof. The vertical extent of this void and the propensity of void-bound material to cave into the tunnel create a challenging ground-control risk, which in this case forced a deviation in the tunneling geometry, as is the reason for the triangular pillar.

Karst void formation occurs as slightly acidic water comes into contact with carbonate rock; the conduits for water flow in this rock mass are the structural discontinuities present due to the folding of the sedimentary layers over geologic time; in the tunnel, as shown in Fig. 2, the discontinuities have been mapped and characterized via LiDAR and geotechnical software

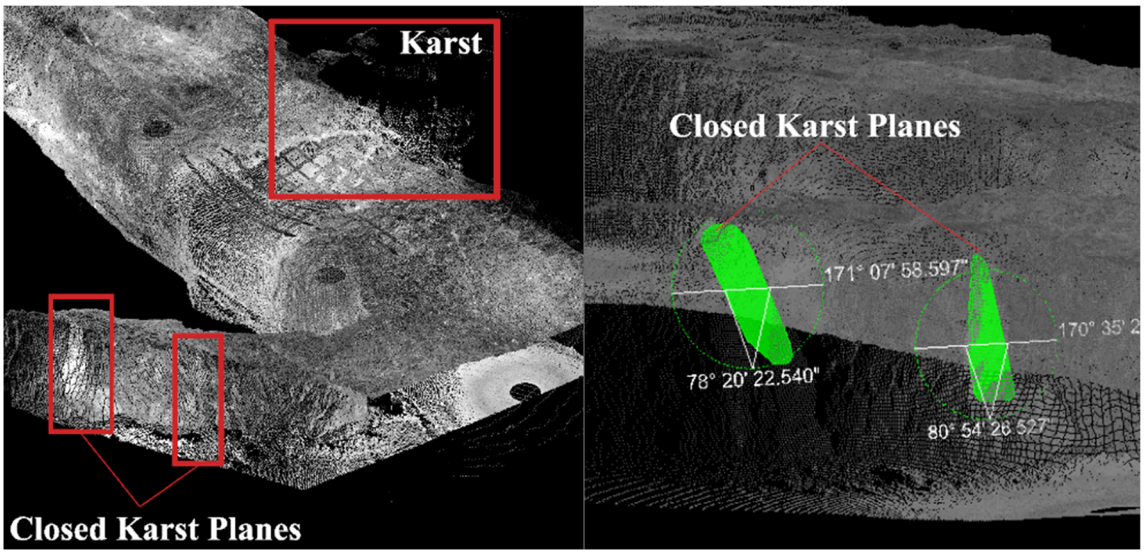

Fig. 5 Dip and dip direction of karst void plane

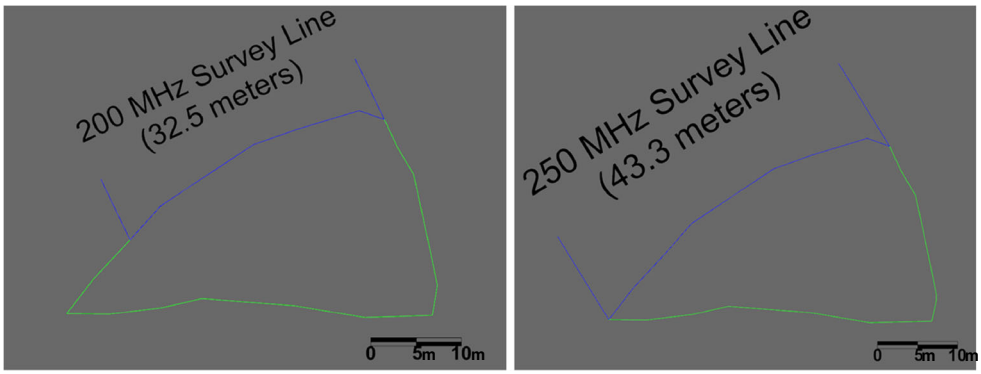

Fig. 7 The 200-MHz and 250-MHz traverse lines

programs in a previous work [15]. That study found four predominant joint sets in the tunnel, including one with a characteristic dip of 88° and a dip direction of 255°; the planar karst cavity in Fig. 2 undoubtedly formed along a fracture represented by that joint set. Figure 3 is a picture taken on the hanging-wall tunnel side of the triangular pillar; steel straps, rock bolts, and plastic mesh were installed in the roof to keep unwanted material from falling into the tunnel. Figure 4 is a picture taken on the foot-wall tunnel side of the triangular pillar, where the only signs of karst void are two closed discontinuities belonging to the previously mentioned joint set with excess residual clay coloring, characteristic of karst voids. Figures 3 and 4 suggest that these two closed discontinuities transition into an open void at some location within the pillar, eventually merging into the massive open void on the hanging-wall tunnel side of the pillar.

The two closed void planes can be seen and characterized from the same laser scan as seen in Fig. 2; using Maptek's I-Site Studio 6.1 software, the dip and dip direction of these planes can be found, as seen in Fig. 5. As suspected, the planes steeply dip at roughly 80°.

The orientation, aperture, and extent of the karst void within the pillar cannot be analyzed visually and cannot be accurately predicted due to the chaotic spatial variance of void sizes throughout the mine. These properties are the targets in the GPR surveys which constitute this study.

2.2 GPR Surveying Underground

A series of two-dimensional GPR surveys were conducted around the triangular pillar at different antenna frequencies to compare depth of penetration and resolution between surveys. The frequencies used were 200 MHz, 250 MHz, 500 MHz, and 1 GHz; all antennas are from Sensors & Software, and all are shielded with the exception of the 200 MHz pulseEKKO antenna. Lower-frequency surveys offer deep penetration with low relative resolution, while higher-frequency surveys offer high resolution at shallow depths. Shielded antennas have a conductive "shield" behind the transmitter and receiver to prevent electromagnetic waves from traveling backwards and to direct energy solely into the desired medium; the use of shielded antennas in a mine tunnel is necessary for accurate data collection, as the rock wall/roof opposite the survey wall/floor is a strong, nearby reflector.

Traditionally, a GPR survey would traverse the ground surface in a straight line, and the shot locations of the survey would be ascertained from GPS systems or by dividing the survey line by the shot spacing of the GPR system. In these case-study surveys, the survey needed to traverse the pillar rib along a line projected onto the irregular pillar surface in an environment with no real-time positioning systems. For the 200-MHz and 250-MHz survey, this was accomplished with a simple surveying ribbon anchored to the rock face, as seen in Fig. 6. The height of the survey was roughly 1 m above the tunnel floor; however, there was a berm with varying heights of material at the foot of the pillar.

The ribbon was marked every 10 cm, which was the step size between signal pulses for both the 200-MHz and 250-MHz surveys. The survey traverse lines are shown in Fig. 7.

Antennas were mounted into a harness apparatus that the researchers fabricated out of PVC. One researcher positioned the two antennas perpendicular to the face along the survey ribbon while the second researcher would manually trigger each radar pulse and alert the first researcher when he could move on to the next mark on the survey ribbon. The survey parameters for 200 MHz and 250 MHz can be seen in Table 1, and the GPR harness can be seen in Fig. 8.

The design for the 500-MHz and 1-GHz surveys was not the same as the 200-MHz and the 250-MHz surveys, as the higher-frequency antennas have smaller spacings along the

Table 1 The 200-MHz and 250-MHz survey parameters

Freq. (MHz)	Survey length (m)	Traces	Points per trace	Antenna spacing (m)	Stacks
200	32.5	324	1875	0.5	32
250	43.3	397	2750	0.25	64

Fig. 8 The 200-MHz survey in progress

survey line (5 cm for 500 MHz, 1 cm for 1 GHz) which make manual-triggering and positioning difficult and prone to operator error. To avoid these inaccuracies, researchers opted for a wheel-trigger to accompany the high-frequency antennas during surveying which would automatically trigger the transmitting antenna based on an odometer. The irregularity of the pillar face was not an ideal track for the wheel-trigger, so 2.4-m-long wooden planks were fixed onto the pillar rib with small anchor bolts and zip-ties, so that the antennas and wheel-trigger would have a smooth, consistent surface to pass-over. The total length of the 500-MHz and 1-GHz surveys was considerably shorter than that of the 200-MHz and 250-MHz survey because of the reduced penetration depth; the surveys were extended only as far as to encompass both of the closed void planes. Also, both the 500-MHz and 1-GHz surveys were divided into multiple 2.4-m-long lines, starting and ending completely on each wooden plank.

As planks were constantly being taken down and put up in the next surveying location, permanent record keeping of plank location and orientation with respect to the pillar rib was required to later ascertain the precise shot locations for the high-frequency surveys. To accomplish this goal, laser scans of the planks were conducted, stitched together, and finally referenced and automatically registered in I-Site Studio 6.0 via reference points to the tunnel point cloud as

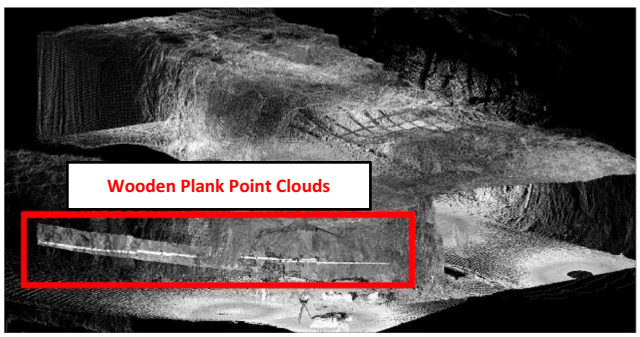

Fig. 9 Planks merged with tunnel

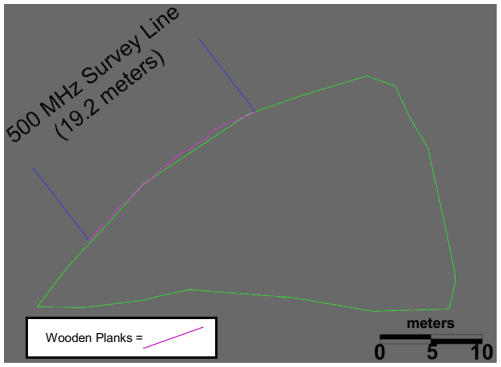

Fig. 10 The 500-MHz traverse lines

shown in Fig. 5. The merged tunnel and plank point clouds can be seen in Fig. 9.

After researchers previewed the 500-MHz data, the 1-GHz survey was designed with two additional plank locations following the final plank location of the 500-MHz survey; this was to try and better image an interesting reflection region seen near the end of the 500-MHz data. The survey traverse lines are shown in Figs. 10 and 11. Corresponding survey parameters for the higher-frequency antennas are shown in Table 2.

3 Data Processing

Data processing was carried out using GPR-SLICE Ground Penetrating Imaging Software. Before any processing or interpretation could occur, point locations for each GPR shot had to be recorded and input into GPR-SLICE along with the raw reflection data. Shot locations were determined by dividing the traverse lines shown in Figs. 7, 10, and 11 by the total number of traces, then exporting the nodes of the divided traverse lines as points in an XYZ format. Pitch and yaw of the antennas were intentionally avoided as much as possible by aligning the antenna faces perpendicular to the survey line, and therefore, were not incorporated into the input location files. Raw radargrams were produced, as shown in Figs. 12, 13, and 14.

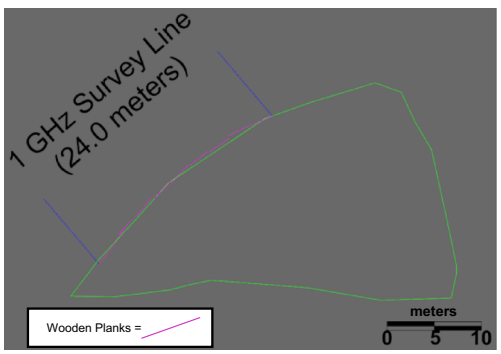

Fig. 11 The 1-GHz traverse lines

Table 2 The 500-MHz and 1-GHz survey parameters

Freq. (MHz)	Survey length (m)	Traces	Points per trace	Antenna spacing (m)	Stacks
500	19.2	398	3300	0.155	16
1000	24.0	2421	2200	0.075	16

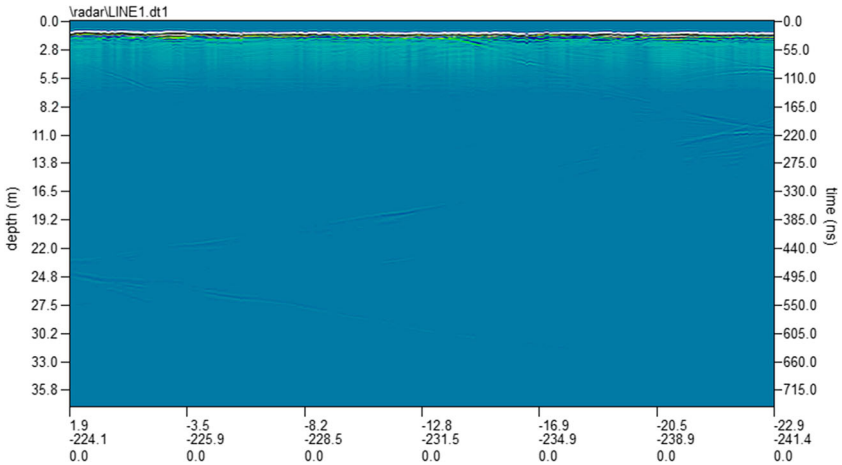

Fig. 12 The 200-MHz raw radargram

The radargrams in Figs. 14 and 15 are the merged individual radargrams for each of the high-frequency wooden plank survey lines. The *y*-axis on all radargrams is time/depth.

3.1 Review of Principles for Interpretation

Speed of the radar wave in a medium is indirectly proportional to the square root of the *dielectric constant* of the medium via the equation:

$$\text{velocity} = \frac{\text{speed of light}}{\sqrt{\text{dielectric constant}}}$$

The dielectric constant is the ratio of the permittivity of a material to the permittivity of free space; limestone has a dielectric constant range of about 4–8 [16]. As there is a common offset between antennas, the estimated depth of reflectors must consider both medium velocity and transmitter-receiver offset:

$$\text{Depth} = \sqrt{\frac{((\text{TwoWay Travel Time})(\text{Velocity}))^2 - \text{Offset}^2}{4}}$$

3.2 Common-Transmitter Survey

Rather than conduct time-consuming permittivity tests on representative core samples, a simple common-transmitter survey on the in-situ rock gives a plot of the direct-wave arrival time versus distance. The design of a common-transmitter survey at the triangular pillar is shown in Fig. 16.

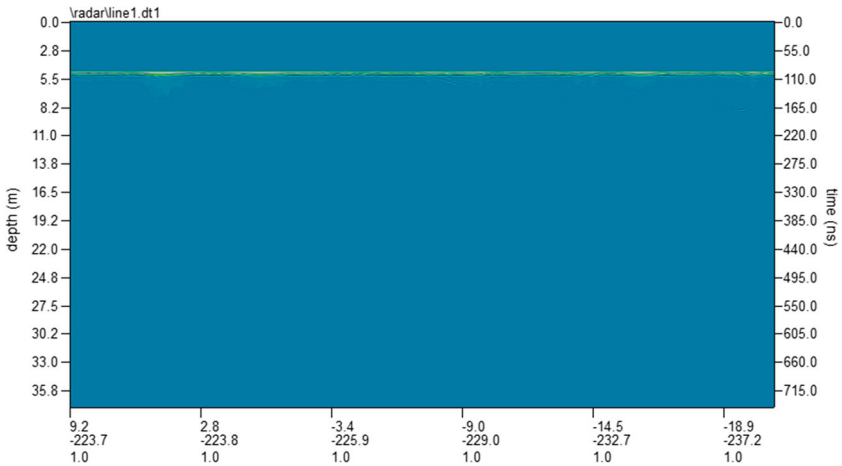

Fig. 13 The 250-MHz raw radargram

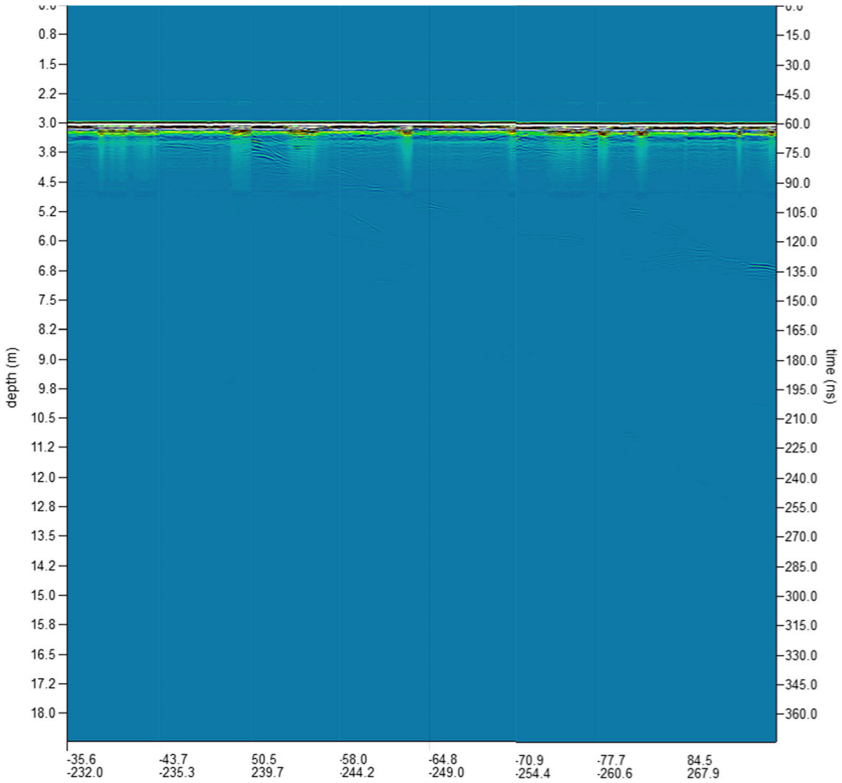

Fig. 14 The 500-MHz raw radargram

The transmitter remained fixed at the indicated location while the receiving antenna was moved from the "start of line" point towards the corner of the pillar. The first arrival wave at the receiving antenna traveled directly from the transmitter in a straight line, and the distance from the transmitter to every receiver position is known; therefore, the velocity of the wave in the pillar can be easily determined. No processing is required for this interpretation, so the radargram displayed by the GPR control console is shown in Fig. 17 with the direct wave indicated.

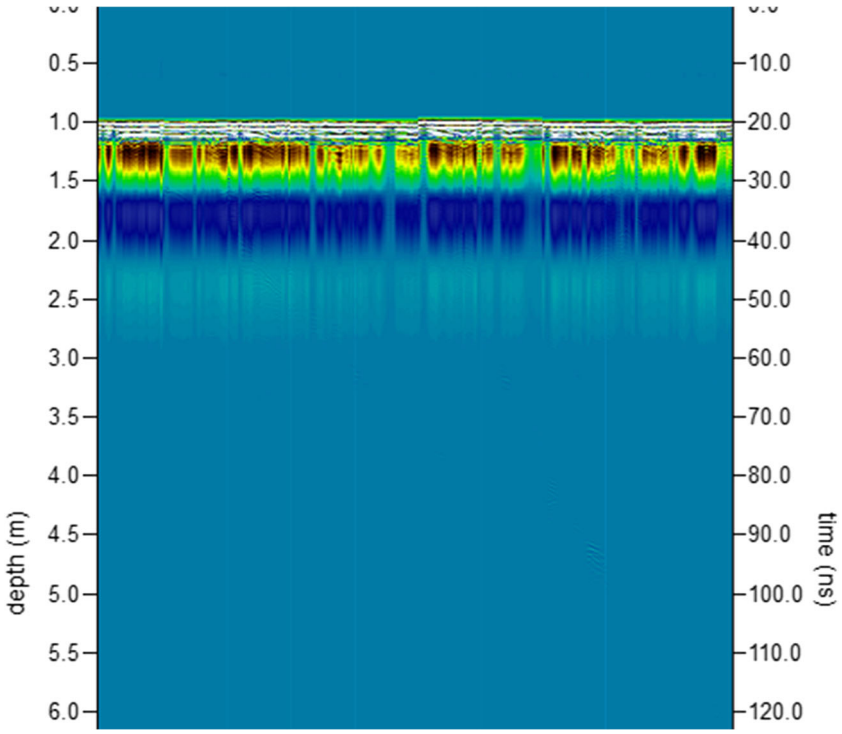

Fig. 15 The 500-MHz (left) and 1-GHz (right) raw radargrams

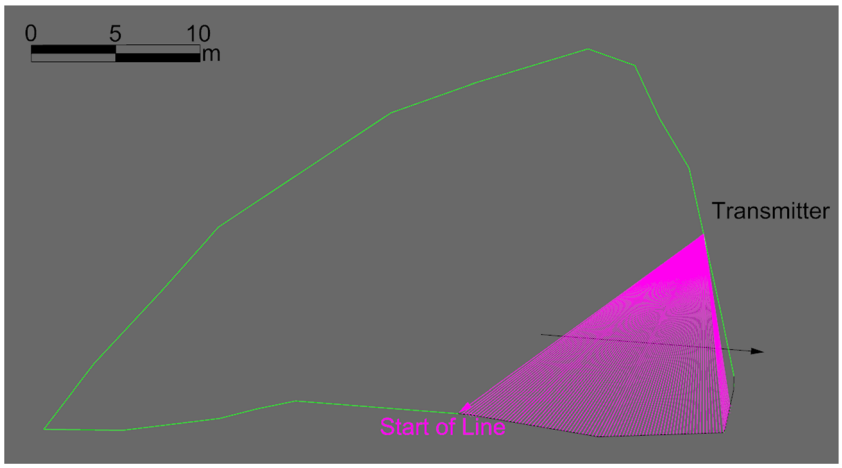

Fig. 16 Common-transmitter survey

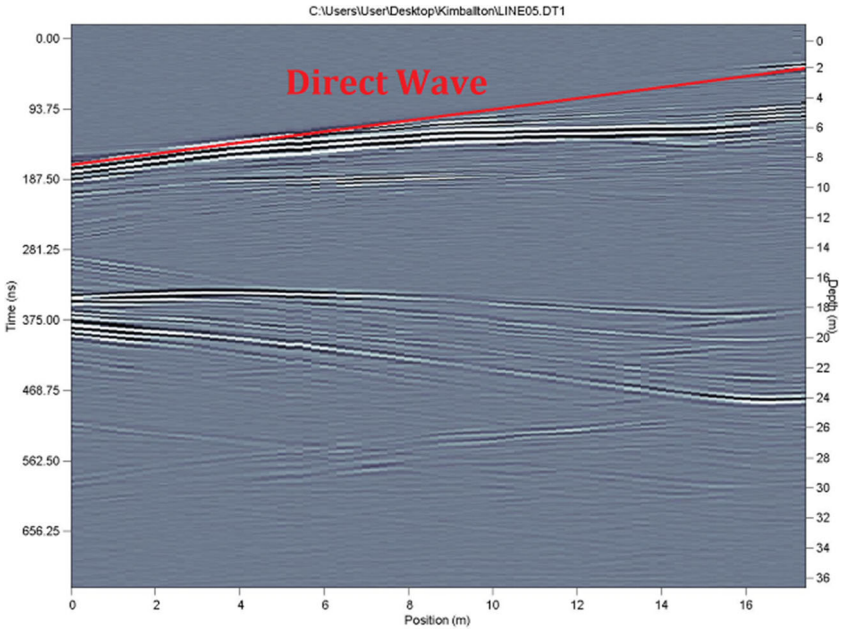

Fig. 17 Common-transmitter survey radargram

The velocity of the radar waves in the case-study pillar was determined to be roughly 0.10 m/ns, which implies a dielectric constant of 9, higher than expected for limestone. The *y*-axis of the reflection radargrams is converted to distance with the value of 0.10 m/ns.

3.3 Processing Flow

As can be seen in Figs. 12, 13, and 15, the raw radargrams showed no discernible reflection horizons and the most part showed nothing; several processing steps were required to correct the time/depth of the data, filter out unwanted frequency responses, apply gain to the signal which attenuates with depth, and filter out other unwanted effects that arise during the surveys. The processing flow applied to these surveys is:

1. Time-zero correction
2. Background filters
3. Bandpass filters
4. Regain (as necessary)

Table 3 Antenna bandwidths

Central frequency (MHz)	Low-end frequency (MHz)	High-end frequency (MHz)
200	100	300
250	125	375
500	250	750
1000	500	1500

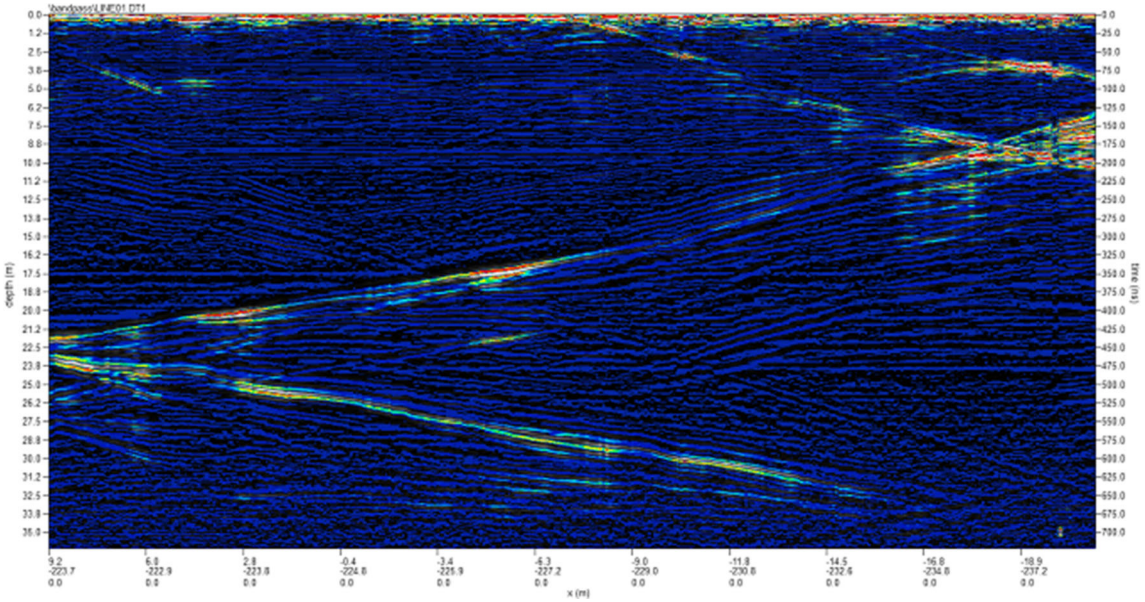

Fig. 18 The 200-MHz time-zeroed, background filtered, bandpass filtered, and gained

The raw radargrams show a gap from time = 0 down towards the consistent horizontal reflection boundary; this boundary is where the radar wave encounters the pillar surface. Within this time range, there is a built-in system delay before the receiving antenna begins recording the reflection data, and the radar wave is actually traveling through air at the speed of light (0.3 m/ns instead of 0.1 m/ns). Furthermore, the desired reflection data lies within the pillar, so the radargrams should be corrected so that time = 0 occurs at the pillar surface reflection boundary. The time-zero corrected radargrams look nearly identical to the raw radargrams, only with all data shifted upwards.

Next, a background filter is applied to each radargram to remove horizontal banding which commonly appears in GPR data as noise from sources such as cellphones or communication networks [21]. The effect of the background filter is largely unnoticeable until gain has been applied. Following the background filter, a bandpass filter is applied to filter out the reflected signal responses with frequencies outside of the operating band of each antenna. The reported frequency for a GPR antenna is actually a central frequency in a bandwidth sent out by the system; the frequency ranges for the four antenna systems used in this case study are shown in Table 3.

Processing gain is applied to the radargrams during the bandpass filtering process. Constant gain can be applied to the entire depth of the radargram; however, it is more appropriate to apply more gain to the signals which have attenuated

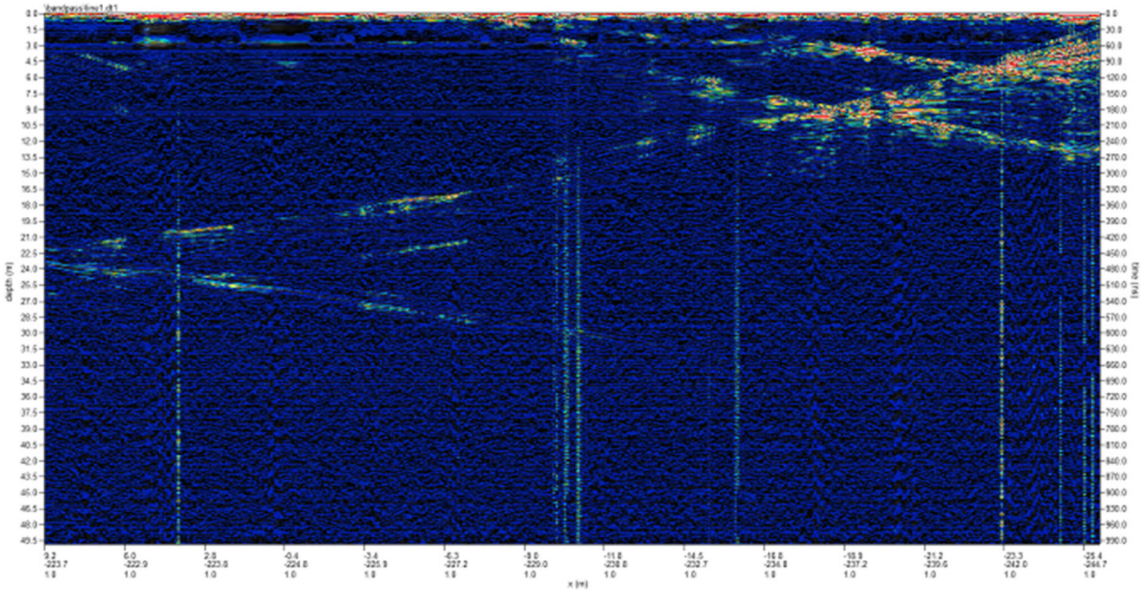

Fig. 19 The 250-MHz time-zeroed, background filtered, bandpass filtered, and gained

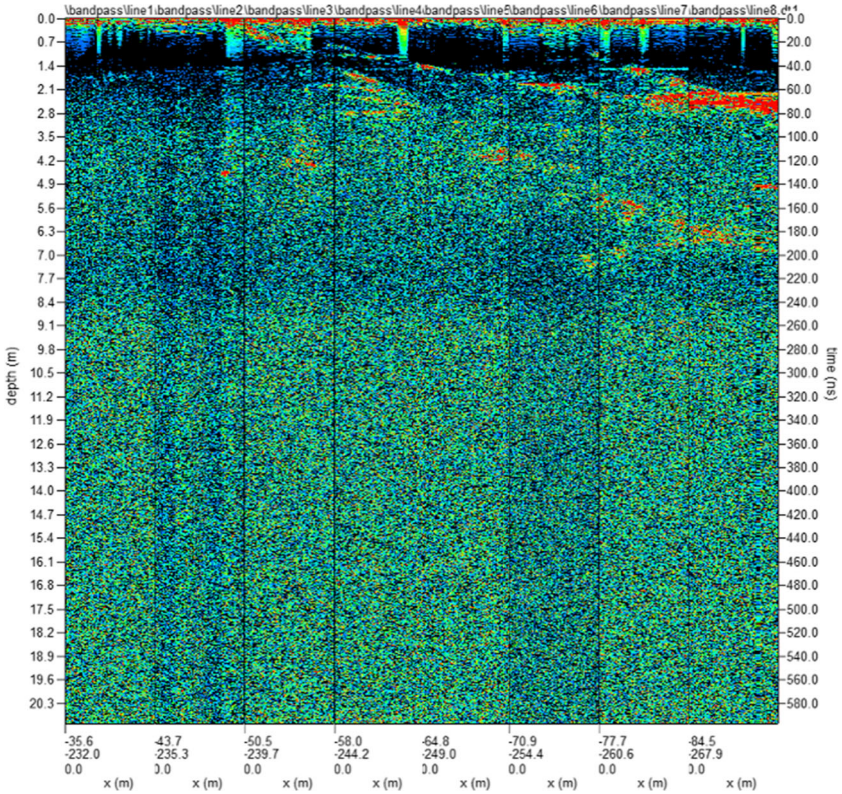

Fig. 20 The 500-MHz time-zeroed, background filtered, bandpass filtered, and gained

more (deeper signals). In GPR-SLICE, a linear, exponential, or custom gain curve can be constructed depending on the expected target depth and attenuation behavior of the radar waves.

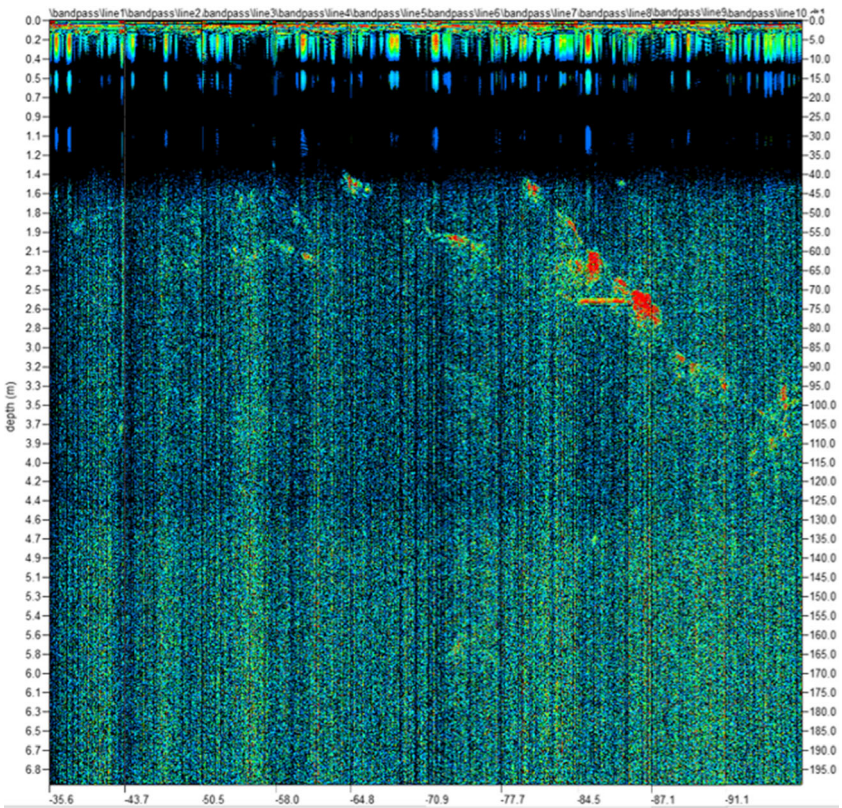

Fig. 21 The 1-GHz time-zeroed, background filtered, bandpass filtered, and gained

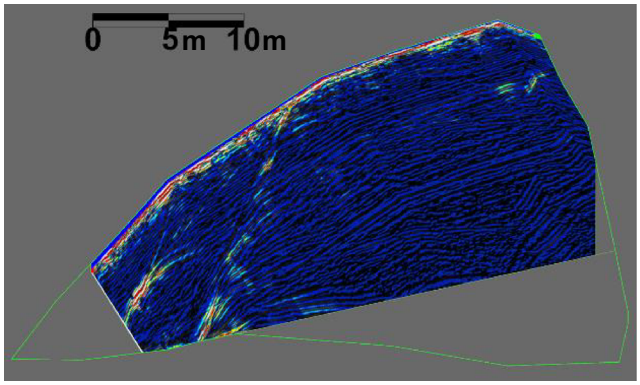

Fig. 22 The 200 MHz in Pillar

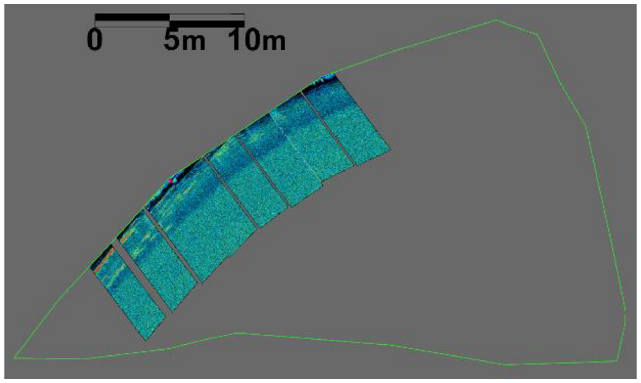

Fig. 24 The 500 MHz in Pillar

4 Results and Discussion

The time-zero corrected, background filtered, bandpass filtered, and gain applied radargrams can be seen in Figs. 18, 19, 20, and 21.

Once the radar data had been fully processed, reflection boundaries became clearly visible in each profile. Across all four frequencies, a dipping reflector towards the end of the radargram was visible; to interpret this consistency and to compare these surveys, they were plotted in their true spatial positions in reference to the pillar geometry. These plots are shown in Figs. 22, 23, 24, and 25.

The previous figures depict how penetration depth reduces as frequency increases; while the 200-MHz and 250-MHz surveys received strong reflection data throughout the pillar (around 11 m depth for good signal), the 500-MHz survey became oversaturated with noise (bad signal) beyond 2.2 m, and the 1-GHz survey encountered the same issue around 1.7 m depth into the pillar. Due to this limitation, neither the 500-MHz nor the 1-GHz surveys were able to detect a consistent linear reflection representative of the karst void planes. Fortunately, both the 200-MHz and 250-MHz surveys show strong reflection boundaries off of two linear features within the pillar. The relevance of these boundaries becomes more obvious when the spatially plotted radargram is plotted with the pillar laser scan in the same view; this depiction is shown in Figs. 26 and 27, where the top half of the foot-wall pillar is cut away to better see the plotted radargram.

The planes suspected to connect to the open karst cavity clearly propagate through the pillar in Figs. 26 and 27. Additionally, the reflection boundaries widen at depth and multiple clustered hyperbolae are seen before the boundaries terminate into the pillar wall. Somewhere in this clustering, the closed planes transition into open fractures and eventually into the open void. Unfortunately, the high-resolution survey quality needed to ascertain these transition locations was not attainable due to the limited depth of penetration for the 500 MHz and 1 GHz. Additional reflection boundaries are visible in the 200-MHz and 250-MHz surveys, one which appears to be a plane connecting the two closed karst void planes.

5 Conclusions

Karst voids may present ground-control risks and hazards associated with water and caving material. The chaotic spatial randomness of karst formation is a

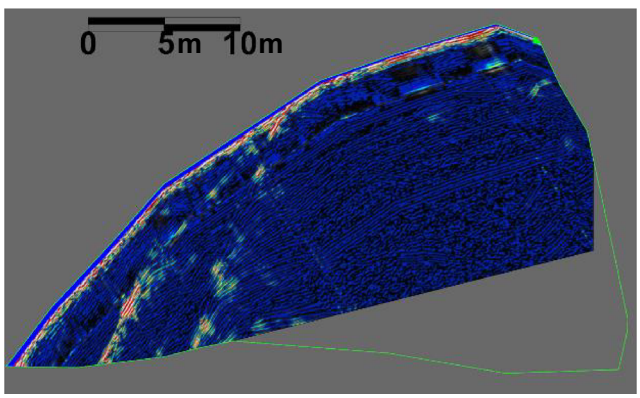

Fig. 23 The 250 MHz in Pillar

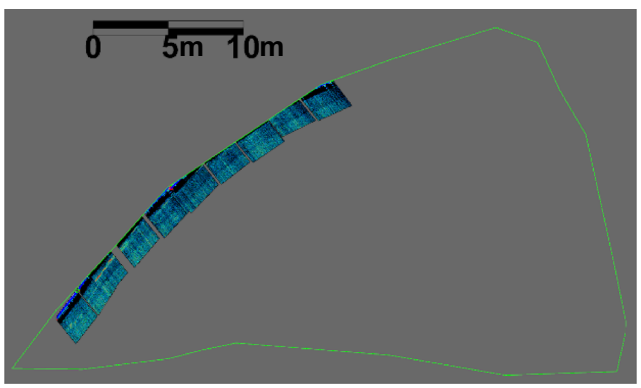

Fig. 25 The 1 GHz in Pillar

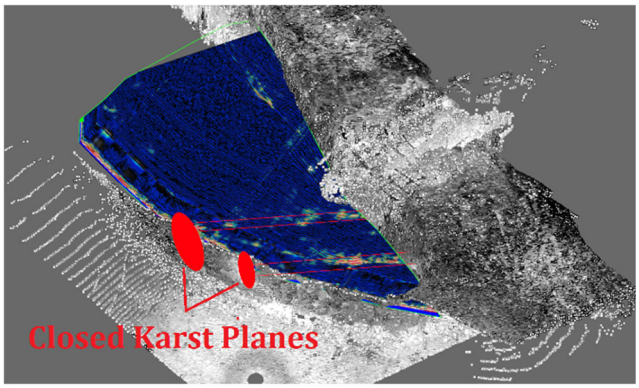

Fig. 26 Radargram spatially in reference to pillar point cloud

challenge for detecting, mapping, and predicting the size of voids. In this work, ground-penetrating radar has been shown to detect karst features within a limestone pillar at depth, and the processed data offers inferences into the locations where these karst features expand into a large open void. The two-dimensional reflection survey has limitations in describing how the karst features are oriented at different heights within the pillar; therefore, multiple surveys are needed to properly describe the karst voids in 3D. Sophisticated analyses, such as gridded 3D surveys on the pillar face, may offer inference into the volume of void space within the pillar.

Using the lower-frequency antennas (200 MHz and 250 MHz), the karst voids were detected as far as about 11 m from the pillar face. This depth of penetration satisfies the case study mine management's need for geologic forecast at an active face of around 5–10 m. While some resolution in the reflected radar waves is not imaged with lower-frequency surveys, the strong dielectric boundary between the limestone pillar and the void space was clearly visible in the 200-MHz and 250-MHz data at depth.

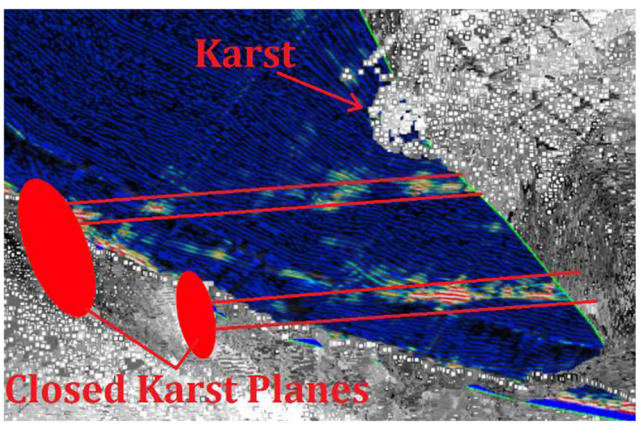

Fig. 27 Close-up view of reflection boundaries

Compliance with Ethical Standards

Conflict of Interest The authors declare that they have no conflict of interest.

References

1. Alija S, Torrijo FJ, Qunita-Ferreira M (2013) Geological engineering problems associated with tunnel construction in karst rock masses: The case of Gaverres tunnel (Spain). Eng Geol 103-111 https://www.researchgate.net/publication/256699865_Geological_engineering_problems_associated_with_tunnel_construction_in_karst_rock_masses_The_case_of_Gavarres_tunnel_Spain
2. Andriani GF, Parise M (2017) Applying rock mass classifications to carbonate rocks for engineering purposes with a new approach using the rock engineering system. Journal of Rock Mechanics and Geotechnical Engineering 364-369 https://www.sciencedirect.com/science/article/pii/S1674775516300981
3. Annan A, Davis JL (1976) Impulse radar sounding in permafrost. Radio Science 383-394 https://ieeexplore.ieee.org/document/7766644
4. Bin L, Zhengyu L, Shucai L, Lichao N, Maoxin S, Huaifeng S, Kerui F, Xinxin Z, Yonghao P (2017) Comprehensive surface geophysical investigation of karst caves ahead of the tunnel face: A case study in the Xiaoheyan section of the water supply project from Songhua River, Jilin, China. Journal of Applied Geophysics 37-49. https://ui.adsabs.harvard.edu/abs/2017JAG...144...37B/abstract
5. Davis J, Annan AP (1989) Ground-Penetrating Radar For High-Resolution Mapping of Soil and Rock Stratigraphy. Geophys Prospect 531-551. https://onlinelibrary.wiley.com/doi/abs/10.1111/j.1365-2478.1989.tb02221.x
6. Eskelinen P, Pellinen T (2018) Comparison of different radar technologies and frequencies for road pavement evaluation. Construction and Building Materials 888-898. https://www.deepdyve.com/lp/elsevier/comparison-of-different-radar-technologies-and-frequencies-for-road-FjD86ngH8n?impressionId=5cd9cf12cdbb3&i_medium=docview&i_campaign=recommendations&i_source=recommendations
7. Grasmueck M (1996) 3-D ground-penetrating radar applied to fracture imaging in gneiss. Geophysics, 1050-1064. https://pubs.geoscienceworld.org/geophysics/article-abstract/61/4/1050/72929/3-D-ground-penetrating-radar-applied-to-fracture?redirectedFrom=fulltext
8. Hasan MI, Yazdani N (2016) An Experimental Study for Quantitative Estimation of Rebar Corrosion in Concrete Using Ground Penetrating Radar. Journal of Engineering 8. https://www.hindawi.com/journals/je/2016/8536850/
9. Hassan N, Zabidi H, Arrifin S, Trisugiwo M (2016) Effect of driling speed of probe drilling data on the clustering of rock strength at NATM-4, Hulu Langat, Selangor. Procedia Chem 19:737–742
10. Kovin ON (2010) Ground penetrating radar investigations in Upper Kama potash mines. Missouri S&T. https://scholarsmine.mst.edu/doctoral_dissertations/2182/
11. Kuniansky EL, Weary DJ, Kaufmann JE (2016) The current status of mapping karst areas and availability of public sinkhole-risk resources in karst terrains of the United States. Hydrogeology 613-624. https://pubs.er.usgs.gov/publication/70160226
12. Leech WD, Jaoude IB, Ghanem N (2008) Madiq Tunnel. TBM Tunneling vs. Karst Geology. Beirut, Lebanon
13. Li S, Li S, Zhang Q, Xue Y, Liu B, Su M, . . . Wang S (2010) Predicting geological hazards during tunnel construction. Journal of Rock Mechanics and Geotechnical Engineering 232-242. https://www.ncbi.nlm.nih.gov/pmc/articles/PMC4706869/

14. Monaghan WD, Trevits MA (2004) Application of ground penetrating radar to evaluate the extent of polyurethane grout infiltration for mine roof control. NIOSH, Pittsburgh
15. Monsalve JJ, Baggett J, Bishop R, Ripepi N (2017) Application of laser scanning for rock mass characterization and discrete fracture network generation in an underground limestone mine. 37th International Conference on Ground Control in Mining, (pp. 183-192). Morgantown, WV.
16. Parkhomenko EI (1967) Eletrical properties of rocks. USSR: Institute of Physics of the Earth, Moscow
17. Simmons G (1972) The surface electrical properties experiment. Lunar Geophysics 258-271. http://citeseerx.ist.psu.edu/viewdoc/download?doi=10.1.1.406.5410&rep=rep1&type=pdf"
18. Slob E, Sato M, Olhoeft G (2010) Surface and borehole ground-penetrating-radar developments. Geophysics:103–120
19. Wang Y, Zhang Z, Ren Q, Wu Y, Peng Z (2012) Application of LTD-2100 ground penetrating radar to advanced forecast in diversion tunnel of jinping hydroelectric power station. 14th International Conference on Ground Penetrating Radar (pp. 57-61). Shanghai: IEEE.
20. Weidong P, Fancheng M, Renguo G, Yonglei L, Zhengbo H (2012) Relationship between operation technology of ground penetrating radar and precision of advanced forecast. International Conference on Computer Science and Electronics Engineering (pp. 640-644). IEEE.
21. Wiseman J, El-Baz F (2007) Remote sensing in archaeology. Springer Science + Business Media, LLC., Boston
22. Zhao C, Li S, Wu J, Xu Z, Zhang Y, Zhou L (2015a) Case study of ground penetrating radar for geological prediction in qiyueshan tunnel. 2nd International Conference on Green Materials and Environmental Engineering, pp. 100-103.
23. Zhao W, Tian G, Forte E, Pipan M, Wang Y, Li X, Shi Z, Liu H (2015b) Advances in GPR data acquisition and analysis for archaeology. Geophys J Int 202:62–71